

Customizable Three-Dimensional-Printed Origami Soft Robotic Joint With Effective Behavior Shaping for Safe Interactions

Juan Yi ¹, Xiaojiao Chen ¹, *Student Member, IEEE*, Chaoyang Song ², Jianshu Zhou ³, *Student Member, IEEE*, Yujia Liu, Sicong Liu ⁴, and Zheng Wang ⁵, *Senior Member, IEEE*

I. INTRODUCTION

Abstract—Fast-growing interests in safe and effective robot–environment interactions stimulated global investigations on soft robotics. The inherent compliance of soft robots ensures promising safety features but drastically reduces force capability, thereby complicating system modeling and control. To tackle these limitations, a soft robotic joint with enhanced strength, servo performance, and impact behavior shaping is proposed in this paper, based on novel three-dimensional-printed soft origami rotary actuators. The complete workflow is presented from the concept of origami design and analytical modeling, joint design, fabrication, control, and validation experiments. The proposed approach facilitates a fully customizable joint design towards the desired force capability and motion range. Validation results from models and experiments using multiple fabricated prototypes proved the excellent performance linearity and superior force capability, with 18.5-N·m maximum torque under 180 kPa, and 300-g self-weight. The behavior shaping capability is achieved by a low-level joint-angle servo and a high-level variable-stiffness regulation; this significantly reduces the impact torque by 53% and ensures powerful and safe interactions. The comprehensive guidelines provide insightful references for soft robotic design for wider robotic applications.

Index Terms—Behavior shaping, customizable design, impact safety, soft robotics, three-dimensional (3-D) printed origami.

Manuscript received March 14, 2018; revised May 28, 2018; accepted August 9, 2018. Date of publication October 4, 2018; date of current version February 4, 2019. This paper was recommended for publication by Associate Editor Jamie Paik and Editor Pierre Dupont upon evaluation of the reviewers' comments. This work was supported in part by Hong Kong RGC-ECS under Grant 27210315, in part by the ITF under Grant ITS/457/17FP, and in part by HKU Seed Funding under Grant 201511159051, Grant 201611159196, and Grant 201711160023. (Juan Yi and Xiaojiao Chen are co-first authors.) (Corresponding author: Zheng Wang.)

J. Yi, X. Chen, J. Zhou, Y. Liu, and Z. Wang are with the Department of Mechanical Engineering, The University of Hong Kong, Pokfulam 999077, Hong Kong (e-mail: yijuan@connect.hku.hk; yji402072495@gmail.com; zhoujs@hku.hk; liu0212@connect.hku.hk; zwangski@hku.hk).

C. Song is with the Department of Mechanical and Energy Engineering, Southern University of Science and Technology, Shenzhen 518055, China (e-mail: songcy@ieee.org).

S. Liu is with the Nanyang Technological University, Singapore 639798 (e-mail: Sliu4@e.ntu.edu.sg).

This paper has supplementary downloadable multimedia material available at <http://ieeexplore.ieee.org> provided by the authors. This includes a video on the performance of SoRA joint, including the concept and prototype of SoRA joint with its motion demonstration and behavior shaping demonstrations, and its sinusoidal signals following test and behavior shaping test. This material is 27.6 MB in size.

Color versions of one or more of the figures in this paper are available online at <http://ieeexplore.ieee.org>.

Digital Object Identifier 10.1109/TRO.2018.2871440

THE safe interaction between robots and environments has received increasing attention in recent years. In particular, robot behaviors to unpredictable impacts attract vast research attention, from motor-driven rigid robots [1], [2] with active impact avoidance and regulation to soft robots [3]–[7] with a passive inherent compliance resulting from flexible materials, mechanisms, or fluidic actuation. Shaping the interaction behaviors of robots, including both passive impact responses and active control, is crucial for robots to conduct normal functionality effectively, while handling unpredictable impacts safely [8], [9]. Compared with rigid robots, soft robots are inherently compliant and adaptable, while considerably reducing the weight and cost. These features of soft robots facilitated their transitions from laboratory prototypes to products [10] for various applications from wearable robots [11]–[13] to surgical robots [14] and manipulators [4]. However, the performance and application of soft robots are hampered by the reduced structural stiffness, limited force capabilities, and challenges in precise modeling and control due to hyperelastic material nonlinearity and complex motion patterns.

Pioneering efforts on soft robotic joints actuated by two antagonistic linear McKibben-type actuators [14]–[18] show promising interaction behaviors with the implementation of PID [19], sliding mode [20], adaptive [21], or model-based controllers [22]. However, the system performances are mainly limited by the McKibben actuators with limited effective force, motion range, and excessive output nonlinearity. Conventional rotary vanes [23] offer another possibility for robotic joint design with inherent compliance from air compressibility, while departing from the closed-chamber design of soft robots leads to their heavy reliance on precision machining and regular servicing. Combining rotary vanes with soft robots, rotary elastic chamber (REC) type actuators have been used in wearable robots showing promising perspectives [24], applying soft bellows into a concise rigid rotary joint. However, limited by the characteristics of bellows, the nonlinearity and the limited effective motion range of REC joints are hard to be overlooked. Recent studies on origami-inspired soft robots [24]–[28] show a promising perspective on easy fast actuation and programmable performance with a simple patterned design and a lightweight body.

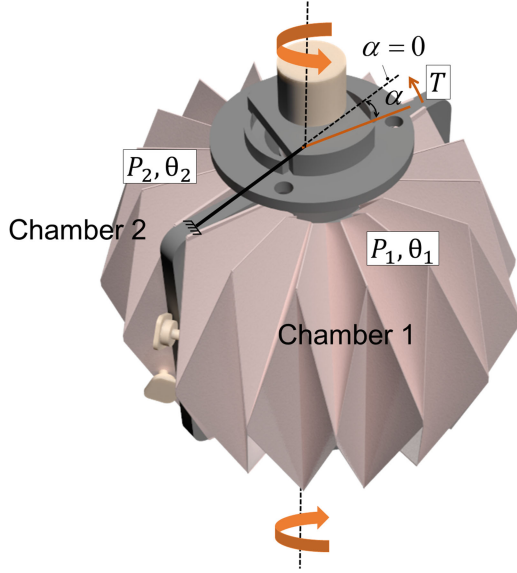


Fig. 1. Concept of SoRA with pressure sensor and encoder embedded. Chambers' pressure P_1, P_2 , chambers' central angles θ_1, θ_2 , and joint angle α are illustrated.

In this paper, we propose an origami soft robotic joint (see Fig. 1) to tackle the aforementioned issues, with three-dimensional (3-D) printed pneumatic soft origami rotary actuators (SoRAs) achieving customizable large force capability, excellent performance linearity, and variable stiffness for effective and safe interactions between robots and unstructured environments.

The main contributions of this paper include: 1) a novel 3-D-printed origami robotic actuator and joint, with design, modeling, and fabrication details validated; 2) detailed quantitative methods of customization to achieve the desired force and motion range; and 3) a hybrid controller with stiffness tuning and interaction control to achieve effective behavior shaping for safe robot–environment interactions. A comprehensive guideline is formulated, from modeling, design, fabrication, and control to customizing a soft robotic joint system.

This paper is organized as follows: The concept and mechanical design of an origami chamber and robotic joint are presented in Section II. Section III presents the modeling work on the robotic system. Experimental validations on fabricated prototypes with static analysis are followed in Section IV. Finally, control performances of position and stiffness towards safe interactions are presented in Section V.

II. CONCEPT OF ORIGAMI AND JOINT DESIGN

A. Origami Concept and Geometric Design

The desirable features of SoRAs, from performance linearity, repeatability, and customizable force and motion to variable joint stiffness and high power-to-weight ratio, are fundamentally enabled by a novel 3-D-printed origami chamber design by using folding and deployment of origami structures with deformation of flexible facets, instead of material inflation for other soft robots, to generate rotary deformation and actuation.

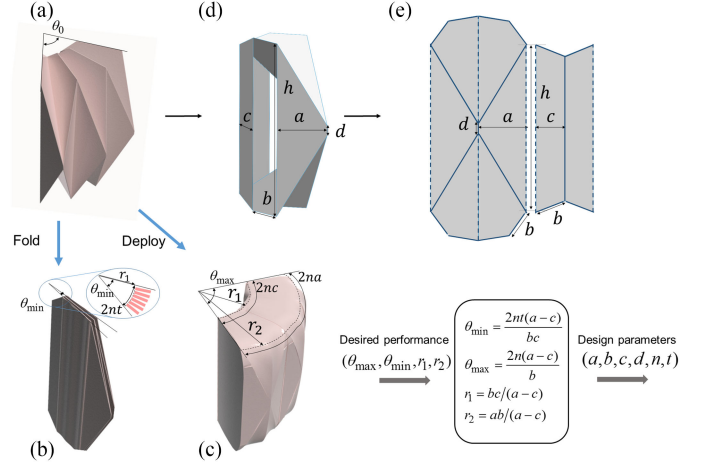


Fig. 2. Concept of the origami chamber. Three working states: (a) NS, (b) FF state, and (c) FD state, together with the (d) geometrics of one unit in the NS and (e) form of the flat sheet.

The proposed design of the origami actuator chamber is achieved by strategically integrating several primitive origami patterns. Studies on origami patterns for the desirable behavior have been well documented [29]–[35]. Engineering applications of origami are mainly focused on three basic patterns: The Yoshimura pattern, the Miura-ori pattern, and the diagonal pattern, which were developed from two basic origami structures [29], namely, the reverse fold (RF) and the accordion fold (AF). While the RF transits from one plane to another by breaking the crease lines, the AF provides a template to combine the multiunits. Our design [see Fig. 2(a)–(c)] takes inspiration from the two basic folding patterns, with three working states under loading, i.e., fully folded (FF), natural state (NS), and fully deployed (FD).

The origami chamber is 3-D-printed in the NS [see Fig. 2(a)] with uniform thickness. It could always return to the NS after actuation. The other two states are shown in Fig. 2(b) and (c) to illustrate the chamber's radial deformation under different pressures. The central angle of the origami chamber in the initial NS is θ_0 , foldable to a minimum of θ_{\min} in the FF with a negative supplied pressure (vacuum) and expandable to a maximum of θ_{\max} in the FD under compression. θ_{\min} and θ_{\max} are crucial in determining the rotary range of the origami chamber. θ_{\min} is determined by the chamber's wall thickness t , as illustrated in Fig. 2(b), and is given by

$$\theta_{\min} = \frac{2nt}{r_1}. \quad (1)$$

The max central angle θ_{\max} depicted in Fig. 2(c) is formulated as follows:

$$\theta_{\max} = \frac{2na}{r_2} = \frac{2nc}{r_1} \quad (2)$$

where r_1 and r_2 are constants of the radius of the origami chamber. r_1 and r_2 can be obtained from geometric functions

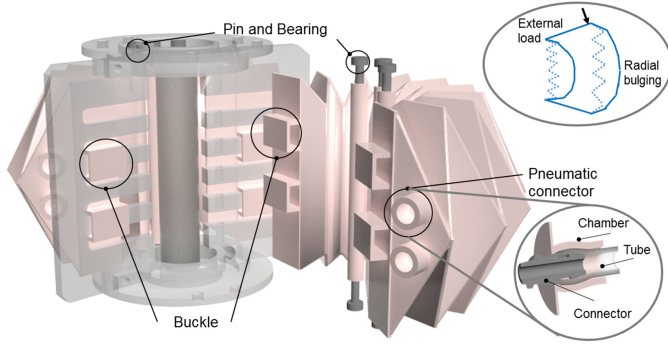


Fig. 3. Exploded view of SoRA with design details.

as follows:

$$\begin{cases} r_2 - r_1 = b \\ \frac{r_1}{r_2} = \frac{c}{a} \end{cases} \quad (3)$$

Therefore, we obtain

$$\begin{cases} r_1 = bc/(a - c) \\ r_2 = ab/(a - c) \end{cases} \quad (4)$$

Substituting (4) into (1) and (2) gives

$$\begin{cases} \theta_{\min} = \frac{2nt(a - c)}{bc} \\ \theta_{\max} = \frac{2n(a - c)}{b} \end{cases} \quad (5)$$

where a , c , b , t , d , and h are characterizing parameters of one unit, from the n identical units as shown in Fig. 2(d). This unit is folded from a flat sheet [see Fig. 2(e)] with illustrated valley folds and mountain folds, which are labeled by dashed and solid lines.

Equations (4) and (5) provide a quantitative guideline for customizing the origami chamber, from a given set of desired performance (θ_{\min} , θ_{\max} , r_1 , r_2) to a corresponding group of design parameters (a , b , c , d , h , t , n) for the origami chamber.

B. SoRA Design

The proposed SoRA joint consists of two antagonistic air-tight origami chambers, a rigid skeleton, and other auxiliary components, including integrated pressure sensors and a rotary encoder. The following features were added, as illustrated in Fig. 3, to improve the air-tightness and performance.

- 1) Motion constraint of the origami chamber: With a large external load opposing the actuation torque, radial bulging (see Fig. 3) will occur. Rigid pins with bearings were added to connect the chamber to the rigid skeleton, as bulging constraints.
- 2) Connection buckles: To ensure a bidirectional force interaction between the chamber and the rigid skeleton, buckles were added to the chamber facades to match the rigid skeleton.
- 3) Pneumatic connection to the chamber: The air inlet is prone to structure distortion at high working pressures. A

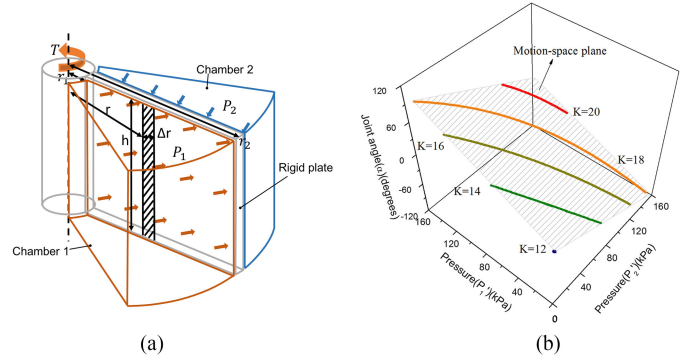


Fig. 4. (a) Diagram of static torque illustration. Chambers 1 and 2 are assumed to inflate to two perfect cylindrical rings during operation. (b) Modeling illustrations on correlations of pressure, joint angle, and joint stiffness. The motion-space plane with oblique lines depicted presents the correlations of joint angles and groups of P_1' , P_2' in free space. Curved lines in the motion-space plane illustrate the constant stiffness as labeled. Unit of stiffness is N-m/rad.

snap-on pneumatic connection with cone screw threads was proposed to ensure air-tightness and easy connection (see Fig. 3).

III. MODELING

This section presents the modeling of the proposed SoRA joint and the corresponding pneumatic actuation system, characterizing the correlations of air pressure, joint position, torque, and variable stiffness.

A. Actuator Modeling

The proposed SoRA joint antagonistically actuates two rotary origami chambers using compressed air for joint rotation and stiffness control. The pressure difference between the two origami chambers (see Fig. 1) causes rotation of the rigid plate with torque T in the working space $[0^\circ, \alpha]$. The joint neutral state ($\alpha = 0^\circ$) is defined as when these two origami chambers are kept in the same state as illustrated. $\alpha > 0^\circ$ when the joint rotates anticlockwise from the neutral state.

Using a cylindrical shape to simplify the inflated origami chamber, Fig. 4(a) illustrates the generated torque, which is given by

$$T = T_1 + T_2 \quad (6)$$

where T_1 and T_2 are the torques generated by Chamber 1 and Chamber 2, which are given by

$$\begin{cases} T_1 = -k\alpha + \int_{r_1}^{r_2} (P_1 - P_0)hrdr \\ T_2 = -k\alpha - \int_{r_1}^{r_2} (P_2 - P_0)hrdr \end{cases} \quad (7)$$

where k is an inherent stiffness constant, which depends on the chamber's material and structure, to be determined by calibration, details of which are discussed in Section V. P_0 is the standard ambient air pressure. Substituting (7) into (6) gives

$$T = -2k\alpha + \frac{h(r_2^2 - r_1^2)}{2}(P_1 - P_2) \quad (8)$$

where h , r_1 , and r_2 are constants from the actuator design. Therefore, full customization of both the motion range and torque can be achieved by following (5) and (8) in the actuator design.

The joint stiffness K is also a critically important factor both for motion control and impact behavior shaping and is defined as follows:

$$K = -\frac{dT}{d\alpha}. \quad (9)$$

Substituting (8) into (9) gives

$$K = -\frac{dT}{d\alpha} = 2k - \frac{h(r_2^2 - r_1^2)}{2} \frac{\partial(P_1 - P_2)}{\partial\alpha}. \quad (10)$$

To calculate $\partial P_1/\partial\alpha$ and $\partial P_2/\partial\alpha$, assuming adiabatic ideal gas [24], we obtain

$$\begin{cases} P_1 = m_1 RT_a / V_1 \\ P_2 = m_2 RT_a / V_2 \end{cases} \quad (11)$$

where R is the specific gas constant, T_a is the absolute temperature of the gas, m_1 and m_2 are the air mass in the origami chambers, and V_1 and V_2 are their volumes, which can be expressed as follows:

$$\begin{cases} V_1 = \theta_1 h(r_2^2 - r_1^2) \\ V_2 = \theta_2 h(r_2^2 - r_1^2) \end{cases} \quad (12)$$

where θ_1 and θ_2 are central angles of Chambers 1 and 2, respectively. θ_1, θ_2 , and α should satisfy the following relations during rotation:

$$\begin{cases} \theta_1 = \pi + \alpha \\ \theta_2 = \pi - \alpha \end{cases}. \quad (13)$$

Combining (11)–(13), $\partial P_1/\partial\alpha$ and $\partial P_2/\partial\alpha$ are calculated as follows:

$$\begin{cases} \frac{\partial P_1}{\partial\alpha} = \frac{\partial P_1}{\partial V_1} \frac{\partial V_1}{\partial\alpha} = -\gamma \frac{P_1}{\pi + \alpha} \\ \frac{\partial P_2}{\partial\alpha} = \frac{\partial P_2}{\partial V_2} \frac{\partial V_2}{\partial\alpha} = \gamma \frac{P_2}{\pi - \alpha} \end{cases} \quad (14)$$

where $\gamma = 1.4$ for air.

Substituting (14) into (10), the stiffness K becomes

$$K = 2k + \gamma \frac{h(r_2^2 - r_1^2)}{2(\pi^2 - \alpha^2)} [\pi(P_1 + P_2) + \alpha(P_2 - P_1)]. \quad (15)$$

Equation (15) describes the correlations of pressure, joint angle, and stiffness, as illustrated in Fig. 4(b). According to (8), in free space, there is a motion-space plane, indicating that the joint angles α correspond to given groups of (P_1', P_2') , where P_1' and P_2' are the relative pressures given by $P_1' = P_1 - P_0$ and $P_2' = P_2 - P_0$. In this motion-space plane, there are evenly spaced curves showing the distribution of K in groups of (P_1', P_2', α) . Variables P_1' and P_2' are unique in achieving the desired joint angle and stiffness.

Finally, a mathematical model revealing the dynamic behavior of the joint system is derived for control purpose using Lagrange's equations of motion as follows:

$$M\ddot{\alpha} + F_f + G + \Gamma = T \quad (16)$$

where M is the inertia matrix, Γ is the external load, F_f is the modeled friction, and $G = mgh \cos \alpha$ is the potential energy of mass m at a height of $h \cos \alpha$ in a gravitational field with constant g . For a preset joint angle and stiffness, solving (15) and (16) yields a unique desired (P_1, P_2) .

B. Air-Flow Dynamics

The air pressures of the two chambers are key variables in the control system. Referring to the well-documented study of air-flow dynamics [36], air pressures can be regulated by controlling the mass flow rate \dot{m} through valves. Thus, we have

$$\dot{m} = \begin{cases} \frac{C_0 AC_1 P_u}{\sqrt{T_a}} & , \frac{P_d}{P_u} \leq 0.528 \\ \frac{C_0 AC_2 P_u}{\sqrt{T_a}} \left(\frac{P_d}{P_u}\right)^{1/\gamma} \sqrt{1 - \left(\frac{P_d}{P_u}\right)^{(\gamma-1)/\gamma}} & , \frac{P_d}{P_u} > 0.528 \end{cases} \quad (17)$$

where the discharge coefficient of the orifice C_0 is a dimensionless constant term in most engineering works, C_1 and C_2 are constants for a given fluid, and P_d and P_u are, respectively, the downstream and upstream pressures in the pneumatic circuit. As a result, transferring from (11), air pressures of the two chambers are given by

$$\begin{cases} \dot{P}_1 = \frac{\gamma RT_a}{V_1} (m_{\text{in}} - m_{\text{out}}) - \frac{\gamma P_1}{V_1} \dot{V}_1 \\ \dot{P}_2 = \frac{\gamma RT_a}{V_2} (m_{\text{in}} - m_{\text{out}}) - \frac{\gamma P_2}{V_2} \dot{V}_2 \end{cases} \quad (18)$$

where m_{in} and m_{out} are, respectively, the mass flow-in and mass flow-out rates through valves, both satisfying the model (17).

Equation (18) reveals the correlations between P and mass flow; it will be used for the lower level pressure control to regulate the mass flow into and out of the actuator.

IV. EXPERIMENT VALIDATION

Models (8) and (15) on the correlations of torque, stiffness, angle, and pressure are validated in this section.

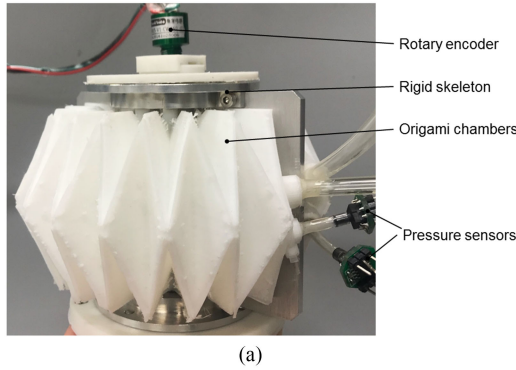
Validation experiments were conducted with SoRA prototypes with a motion range $\alpha \in [-60^\circ, 60^\circ]$. Dimensions are listed in Table I. In this prototype, the rigid skeleton was made with aluminum alloy. Origami chambers were fabricated by a 3-D printer (Delta-bot consumer grade 3-D-printer) based on fused deposition modeling with flexible thermoplastic polyurethane. A uniform wall thickness of 1.3 mm was sufficient to achieve air-tightness. Key printing parameters are noted, which are as follows: Printing speed (10 mm/s), layer height (0.08 mm), and fill density (100%). The finished prototype is shown in Fig. 5(a).

Coping with the unique performance and characteristics of soft robots, a dedicated experiment platform was developed to test SoRAs, as shown in Fig. 5(b). A horizontal rotary table was mounted to provide manual rotation, where a torque sensor

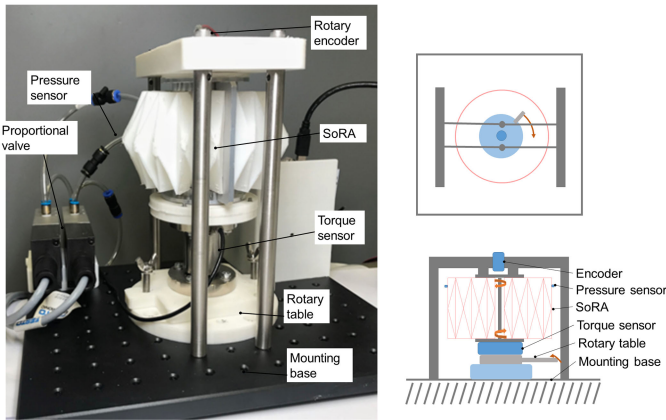
TABLE I
SoRA DIMENSIONS

Symbol	Quantity	Values
t	wall thickness	1.3mm
h	height	65mm
r_1	inner radius	30mm
r_2	outer radius	55mm
θ_{\min}	chamber minimum central angle	120°
θ_{\max}	chamber maximum central angle	240°
α	joint angle	$[-60^\circ, 60^\circ]$

mm = millimeter, ° = degree.



(a)



(b)

Fig. 5. (a) Prototype of SoRA with sensors embedded. (b) Experimental platform with the SoRA mounted for static tests. The top cap of the SoRA was fixed to the mounting base. The bottom cap of the SoRA can be manually rotated by connecting to the rotary table.

(-20 to 20 N·m, accuracy: 1%) was connected to the bottom cap of a SoRA to measure the torque. The top cap of the SoRA was fixed to the mounting base. With this configuration, the joint could either be manually rotated or be fixed at a constant joint angle. The joint was embedded with a rotary encoder (0 – 360° , accuracy: 0.5%) and two pressure sensors (0 – 200 kPa, accuracy: 0.5%). At the air inlet, two proportional valves (Festo MPYE 5/3-way) were used to regulate the input pressure. Therefore, real-time regulation and measurement of chamber pressure, joint torque, and joint angle could be achieved from this platform.

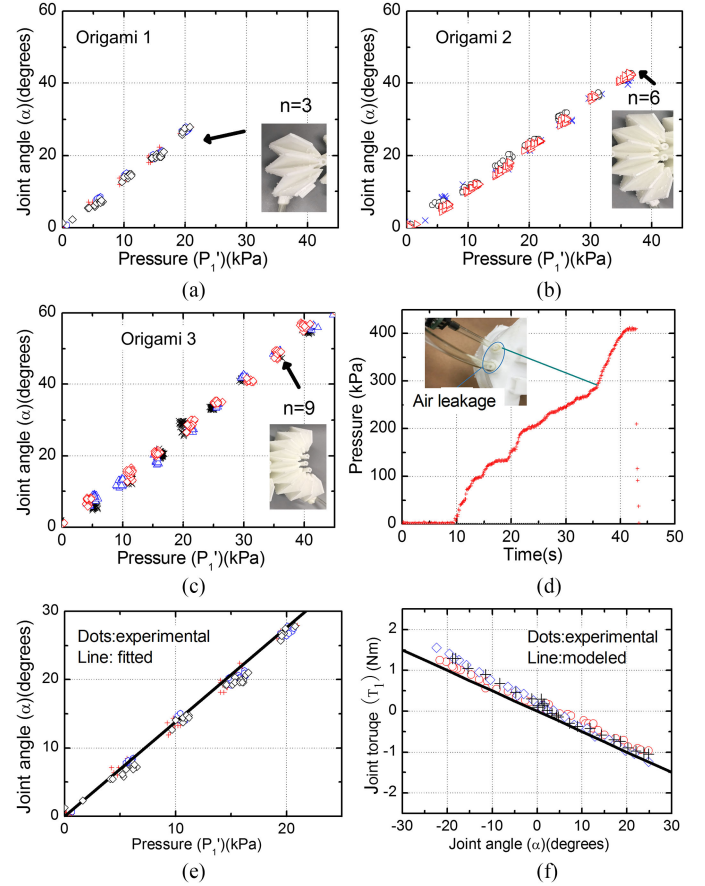


Fig. 6. Origami chamber static test results. (a–c) Performance repeatability test: Origami 1, Origami 2, and Origami 3. Each test was repeated three times. (d) Maximum withstanding pressure of the origami chamber. (e), (f) k calibration and validation tests.

A. Origami Chamber: Repeatability Test

The performance repeatability, as an important characteristic for an actuator, especially for a 3-D-printed soft actuator, was validated. Three types of origami chambers [see Fig. 6(a)–(c)], i.e., Origamis 1, 2, and 3, with the same unit parameters ($a = 13$ mm, $b = 15$ mm, $c = 10$ mm, $d = 5$ mm), same material parameters ($t = 1.3$ mm), and different unit numbers ($n = 5, 7, 9$, respectively) were tested in the platform. These chambers were actuated in free space during the test. With the change of input pressure P_1' , the joint angle increased. The input pressure and joint angle were recorded. Each test was repeated three times.

The experimental results are shown in Fig. 6(a)–(c), where a linear relation between the input pressure and the angle of Origamis 1, 2, and 3 is exhibited. Multigroups of overlapped lines illustrate the high performance repeatability of 3-D-printed origami chambers. In addition, these three chambers followed very similar pressure–angle tendency that the motion range increased with increasing n . This tendency agreed with the relations of θ_{\max} and n revealed in model (5). Therefore, origami chambers can be customized to the desired motion range by selecting n .

The maximum withstanding pressure of the origami chambers was also tested in free space with gradually increased air

pressures from 0 kPa. As shown in Fig. 6(d), the origami chambers with 1.3-mm wall thickness could withstand around 300-kPa pressure before air leakage occurred in the pneumatic connector. The main chamber body could withstand at least 400 kPa in further tests [see Fig. 6(d)] inspite of the leakage at the connection point, suggesting potentials for further development.

B. Origami Chamber: Inherent Stiffness Calibration

A SoRA with Origami 1 (see Fig. 6) was utilized in the calibration test to obtain and validate the inherent stiffness constant k .

Following the same experimental procedure as the repeatability test, the calibration test results were obtained and are depicted in Fig. 6(e), with line-fitting. Referring to (7), the stiffness constant k can be obtained by calculating the slope of the function at $T_1 = 0$, which was calculated as $k = 2.87$ N·m/rad.

Further experiments were conducted to validate the stiffness constant k obtained from the calibration. Origami 1 was kept at standard air pressure, i.e., $P_1' = 0$ kPa. The joint was manually rotated to record the exerted joint torques with varying angles. Experimental results are depicted in Fig. 6(f). The modeled results obtained by substituting k into (7) are also illustrated in the figure. Agreements between experimental and modeled results can be observed with a mean error of 0.20 N·m. Therefore, the estimated $k = 2.87$ N·m/rad can be used in the following study.

C. SoRA: Free-Space Test

A SoRA with Origami 3 (see Fig. 6) was chosen with the largest motion range. Experiments were performed to validate the joint static performances. Free-space tests were conducted to validate the correlations of joint angle and pressure. During the test, the pressure of Chamber 2 was maintained at the ambient air pressure, while Chamber 1 was actuated to drive the joint. Relations between angles and pressure are illustrated in Fig. 7(a), where the modeled results show excellent agreements with the experimental results with a mean error of 1.52° . A maximum angle of 60° was achieved by actuating Chamber 1. Since Chambers 1 and 2 had identical geometry, the SoRA is capable of rotating in the proposed motion range $[-60^\circ, 60^\circ]$. The motion demonstration of the SoRA joint in free space is shown in the supplementary video.

D. SoRA: Static Torque Test

The force capability of the joint was investigated in this experiment. Equation (10) of static torque, chamber pressure, and actuator dimensions was verified. Torque tests were conducted to record the static torque under variable angle and air pressure conditions.

The actuator joint angle was kept constant during the test. Chamber 2 was connected to the atmosphere and kept at the standard pressure $P_2' = 0$ kPa, while increasing pressure P_1' of Chamber 1. Joint torques were recorded. In this experiment, five constant angles ($\alpha = -60^\circ, -45^\circ, 0^\circ, 45^\circ$) were set to validate model (8). Tests in each set were repeated three times.

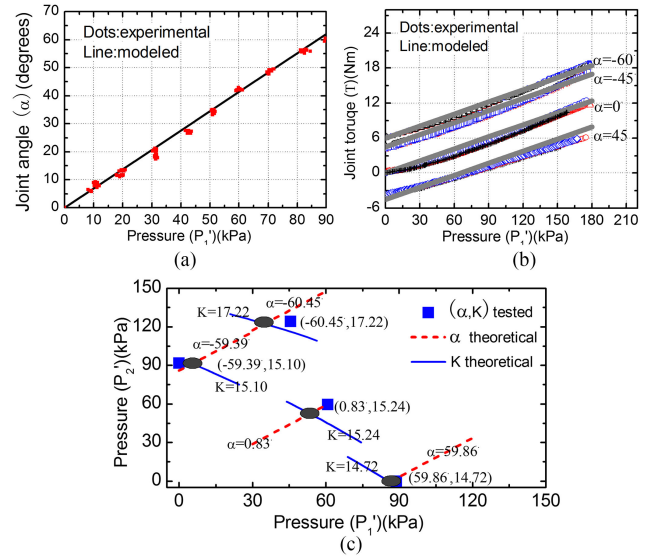


Fig. 7. SoRA static test results. (a) SoRA free-space test. (b) SoRA static torque test. (c) SoRA variable stiffness test. Solid squares with illustration denote the *actual* angle and stiffness at given pressures. The modeled results corresponding to the experimental results are indicated as follows: α : dash line, K : solid line, and intersecting circles: modeled results.

Relations between torque and pressure for different joint angles are depicted in Fig. 7(b). The measured and modeled joint torques for $\alpha = -60^\circ, -45^\circ, 0^\circ, 45^\circ$ were in good agreement with mean errors of 0.61, 0.64, 0.48, and 0.69 N·m, respectively. The joint torques proportionally increased with increasing pressures for constant angles, reaching the maximum torque of 18.5 N·m at $P_1' = 180$ kPa, $P_2' = 0$ kPa, and $\alpha = -60^\circ$.

Considering the light self-weight of the origami chamber (70 g) and the weight of the SoRA joint (300 g), a much higher torque-to-weight ratio was achieved, compared with commercial servo motors (e.g., AKMServo by Kollmorgen, peak torque: 7.2 N·m, weight: 2.9 kg [37]). Slight deviations were observed between the experimental and modeled results, possibly caused by the energy loss in structural deployment, which could be compensated for in the controller discussed in Section V.

E. SoRA: Variable Stiffness Test

With the proposed robotic joint, as derived in (15), variable stiffness could be achieved by varying P_1 and P_2 for various angles α . To verify model (15), we tested the variable stiffness by recording joint torques and angles. Experiments were performed with closed valves and a constant mass of air held inside each chamber. The experimental procedure consisted of three steps: 1) each chamber was supplied with corresponding pressures to move the joint to the target angle in free space; 2) two valves were closed to maintain constant air mass in both chambers; and 3) an external force was applied to the forearm to rotate it at 10° , with the required torque measured. The joint stiffness was obtained by calculating the ratio of the measured torque to the given angle difference, i.e., 10° .

Joint angles and calculated stiffness values for different P_1' and P_2' values are shown in Fig. 7(c), where solid squares denote the *actual* joint angle and stiffness at the corresponding

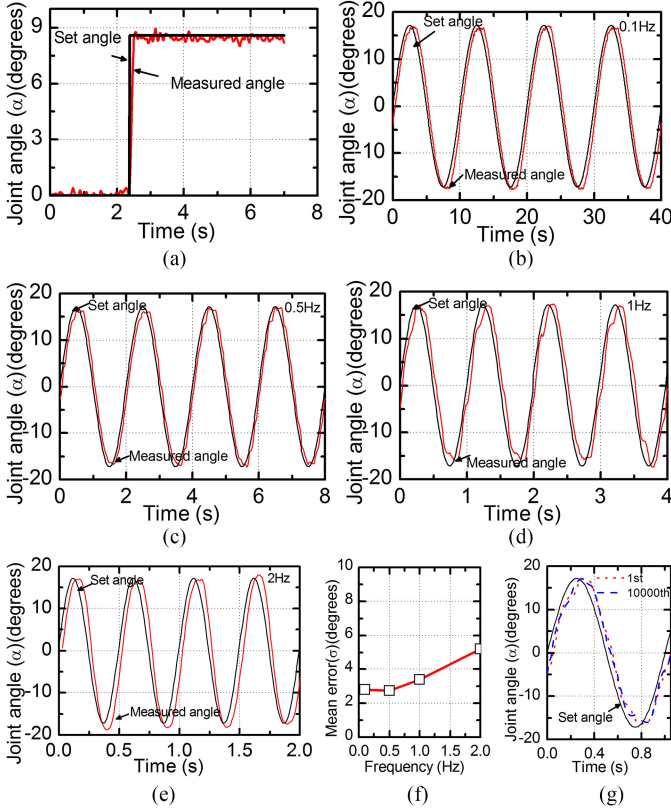


Fig. 9. Controller tests. (a) Step response test results. (b–e) Sinusoidal test results for 0.1, 0.5, 1, and 2 Hz. (f) Angle mean error at the tested reference signal frequencies. (g) Cycling test results showing the sinusoidal function following performance before and after the cycling test.

control. In this test, the joint was initially held at $\alpha = 0^\circ$; a sudden impact was simulated of the block falling freely from the same height under three conditions, i.e., fully fixed state ($K = \infty, \alpha = 0^\circ$), actuated state ($K = 15, \alpha = 0^\circ$), and free-space state ($K = 5.7, \alpha = 0^\circ$). The joint was fixed with bolts in the fully fixed state. In the actuated state, Chambers 1 and 2 were set to the desired stiffness. In the free-space state, both chambers were kept at standard air pressure. The impact torques were recorded by the torque sensor on the joint; each test was repeated three times. The experimental results, as plotted in Fig. 10(a), indicated that, compared with the fully fixed state, the additional compliance could significantly reduce the torque during impact. As shown in Fig. 10(b), the peak torque could be maximally reduced by as much as 53% from 4.7 to 2.5 N·m.

The second test was focused on validating the ability of the hybrid cascaded controller with both high-level and low-level control. The same procedure as for the first test was repeated but with the active PID angle control turned-ON. Fig. 10(c) shows the desired angle, the measured angle, the desired stiffness, and the measured stiffness, with the impact occurring at 3.06 s, which resulted in a sudden angle variation of 7.3° and further affected the pressure of the two chambers. The differences in the reaction speed were clearly demonstrated here. When the impact torque peaked after 0.2 s, the active controller took 0.9 s to recover and restore to the original state. Compared with the results from the first test, although the active PID controller was slower than the

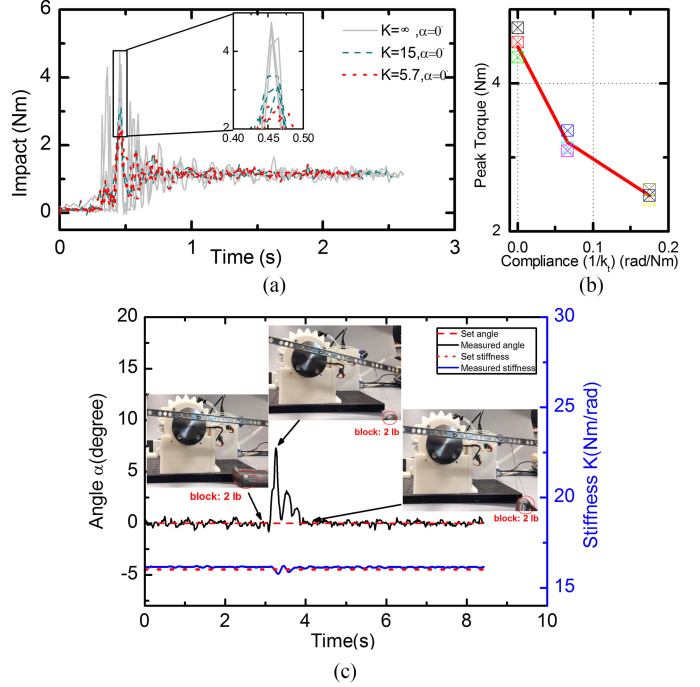


Fig. 10. Behavior shaping tests. (a) Passive impact reduction test results. The joint torque compared between a fixed joint at $\alpha = 0^\circ$ and a joint with a preset stiffness of $K = 15$. The peak impact torque could be reduced by 40%, but without the active angle control, the joint angle could not be restored. (b) Relations between the stiffness and impact. (c) Hybrid control with passive stiffness and active regulation; disturbance could be restored by returning to the original angle.

passive stiffness preset, it could successfully restore the joint from the impact disturbance back to the desired angle.

In summary, combining passive stiffness presetting and active PID cascade control, the proposed SoRA joint exhibits distinctive characteristics for impact response and disturbance rejection, similar to the impedance control for rigid admittance-type robotic manipulators. However, the soft robotic approach differs fundamentally from rigid robots in that the passive stiffness setting generated the fastest and, hence, the most fundamental impact response, while for rigid robots the high-speed PID control loop dominated all subsequent high-level behaviors. The results presented in this paper are only preliminary. Future works will investigate further towards efficient impact behavior shaping for soft robots.

VI. CONCLUSION AND FUTURE WORK

This paper presented the design, modeling, fabrication, and control of a novel pneumatic soft origami robotic joint showing substantially improved payload, performance linearity, and variable stiffness with effective behavior shaping for safe robust effective robot–environment interactions. These features were primarily facilitated by the proposed soft 3-D-printed origami chamber with a high payload of 18.5 N·m at 180-kPa actuation pressure and a completely customizable design towards performance indices. Analytical models for the customizable origami chamber design to achieve the desired force capability and motion range were provided. The linearity and relations between

joint torque, angle, and pressure were modeled and validated on a proprietary experimental platform. An experimental validation of the variable stiffness modeling of the joint was conducted. A hybrid cascaded controller with active angle and stiffness control was developed and implemented onto the joint system, achieving a high angle servo accuracy of 0.3° , a large bandwidth of 2 Hz, fast response speed within 0.3 s, and impact behavior shaping, reducing the impact torque by 53%, while preserving impact restoration capabilities. A lifecycle test was conducted on the SoRA prototype, with over 10 000 full actuation cycles without failure.

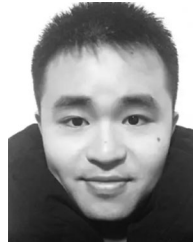
Although the approach of a robot joint driven by antagonistic inflatable chambers was proposed decades ago using rubber or plastic bellows, in this study, the proposed origami design approach and the 3-D-printing fabrication method provided substantially new insights. Not only can the proposed SoRA joints be strong, precise, and responsive, they can also be PID-controlled to follow fast-changing desired trajectories. Moreover, by adopting the origami approach, the performance of the SoRA joint could be customized by mechanical design, with the guideline models readily provided in this study. In the end, the impact behavior shaping enabled by the SoRA joint's excellent performance was formulated by the proposed hybrid SoRA controller and validated by experiment results, showing that the SoRA joint could offer an inherently safe impact response combined with active disturbance rejection tuned according to applications. This enables new behavior-shaping possibilities for soft robots, where unintended impacts can be seamlessly integrated into controller synthesis, without affecting the normal working conditions, enabling safe and effective robotic operation within unknown and uncertain environments.

Future work will investigate the behavior-shaping potentials of soft robots, exploring the applications of the proposed joint system in various environments, as well as further developments of the proposed SoRA joint into multiple DOF robotic systems. System actuation speed and control will also be investigated towards improved performances for interaction and manipulation applications.

REFERENCES

- [1] F. L. Lewis, D. M. Dawson, and C. T. Abdallah, *Robot Manipulator Control: Theory and Practice*. New York, NY, USA: Marcel Dekker Inc., 2003.
- [2] A. J. Critchlow, *Introduction to Robotics*. New York, NY, USA: Macmillan, 1985.
- [3] D. Rus and M. T. Tolley, "Design, fabrication and control of soft robots," *Nature*, vol. 521, no. 7553, 2015, Art. no. 467.
- [4] T. George Thuruthel, Y. Ansari, E. Falotico, and C. Laschi, "Control strategies for soft robotic manipulators: A survey," *Soft Robot.*, vol. 5, no. 2, pp. 149–163, 2018, doi: [10.1089/soro.2017.0007](https://doi.org/10.1089/soro.2017.0007).
- [5] G. Grioli *et al.*, "Variable stiffness actuators: The users point of view," *Int. J. Robot. Res.*, vol. 34, no. 6, pp. 727–743, 2015.
- [6] Z. Wang, M. Z. Chen, and J. Yi, "Soft robotics for engineers," *HKIE Trans.*, vol. 22, no. 2, pp. 88–97, 2015.
- [7] H. R. Choi *et al.*, "Biomimetic soft actuator: Design, modeling, control, and applications," *IEEE/ASME Trans. Mechatronics*, vol. 10, no. 5, pp. 581–593, Oct. 2005.
- [8] B. Vanderborght *et al.*, "Variable impedance actuators: A review," *Robot. Auton. Syst.*, vol. 61, no. 12, pp. 1601–1614, 2013.
- [9] J. E. Colgate and N. Hogan, "Robust control of dynamically interacting systems," *Int. J. Control*, vol. 48, no. 1, pp. 65–88, 1988.
- [10] D. P. Holland *et al.*, "The soft robotics toolkit: Strategies for overcoming obstacles to the wide dissemination of soft-robotic hardware," *IEEE Robot. Automat. Mag.*, vol. 24, no. 1, pp. 57–64, Mar. 2017.
- [11] P. Polygerinos, Z. Wang, K. C. Galloway, R. J. Wood, and C. J. Walsh, "Soft robotic glove for combined assistance and at-home rehabilitation," *Robot. Auton. Syst.*, vol. 73, pp. 135–143, 2015.
- [12] Z. Wang, P. Polygerinos, J. T. Overvelde, K. C. Galloway, K. Bertoldi, and C. J. Walsh, "Interaction forces of soft fiber reinforced bending actuators," *IEEE/ASME Trans. Mechatronics*, vol. 22, no. 2, pp. 717–727, Apr. 2017.
- [13] J. Yi, X. Chen, and Z. Wang, "A three-dimensional-printed soft robotic glove with enhanced ergonomics and force capability," *IEEE Robot. Automat. Lett.*, vol. 3, no. 1, pp. 242–248, Jan. 2018.
- [14] T. Ranzani, M. Cianchetti, G. Gerboni, I. De Falco, and A. Menciassi, "A soft modular manipulator for minimally invasive surgery: Design and characterization of a single module," *IEEE Trans. Robot.*, vol. 32, no. 1, pp. 187–200, Feb. 2016.
- [15] B. Tondu, "Modelling of the Mckibben artificial muscle: A review," *J. Intell. Mater. Syst. Struct.*, vol. 23, no. 3, pp. 225–253, 2012.
- [16] B. Tondu and P. Lopez, "Modeling and control of Mckibben artificial muscle robot actuators," *IEEE Control Syst. Mag.*, vol. 20, no. 2, pp. 15–38, Apr. 2000.
- [17] D. G. Caldwell, G. A. Medrano-Cerda, and M. Goodwin, "Characteristics and adaptive control of pneumatic muscle actuators for a robotic elbow," in *Proc. IEEE Int. Conf. Robot. Automat.*, 1994, pp. 3558–3563.
- [18] J. Yi, X. Chen, C. Song, and Z. Wang, "Fiber-reinforced origami robotic actuator," *Soft Robot.*, vol. 5, no. 1, pp. 81–92, 2018, doi: [10.1089/soro.2016.0079](https://doi.org/10.1089/soro.2016.0079).
- [19] S. Ganguly, A. Garg, A. Pasricha, and S. Dwivedy, "Control of pneumatic artificial muscle system through experimental modelling," *Mechatronics*, vol. 22, no. 8, pp. 1135–1147, 2012.
- [20] H. Aschemann and D. Schindele, "Sliding-mode control of a high-speed linear axis driven by pneumatic muscle actuators," *IEEE Trans. Ind. Electron.*, vol. 55, no. 11, pp. 3855–3864, Nov. 2008.
- [21] G. A. Medrano-Cerda, C. J. Bowler, and D. G. Caldwell, "Adaptive position control of antagonistic pneumatic muscle actuators," in *Proc. IEEE/RSJ Int. Conf. Intell. Robots Syst. Human Robot Interact. Cooperative Robots*, vol. 1, 1995, pp. 378–383.
- [22] S. V. Krichel, O. Sawodny, and A. Hildebrandt, "Tracking control of a pneumatic muscle actuator using one servovalve," in *Proc. IEEE Amer. Control Conf.*, 2010, pp. 4385–4390.
- [23] Festo Company, Germany. Rotary Vane. 2017. [Online]. Available: <http://www.festo.com>. Accessed on: Jan. 2018.
- [24] O. Ivlev, M. Mihajlov, and A. Graser, "Modular multi-sensory fluidic actuator with pleated rotary elastic chambers," *IFAC Proc. Volumes*, vol. 39, no. 16, pp. 271–276, 2006.
- [25] C. D. Onal, R. J. Wood, and D. Rus, "Towards printable robotics: Origami-inspired planar fabrication of three-dimensional mechanisms," in *Proc. IEEE Int. Conf. Robot. Automat.*, 2011, pp. 4608–4613.
- [26] C. D. Onal, R. J. Wood, and D. Rus, "An origami-inspired approach to worm robots," *IEEE/ASME Trans. Mechatronics*, vol. 18, no. 2, pp. 430–438, Apr. 2013.
- [27] R. V. Martinez, C. R. Fish, X. Chen, and G. M. Whitesides, "Elastomeric origami: Programmable paper–elastomer composites as pneumatic actuators," *Adv. Functional Mater.*, vol. 22, no. 7, pp. 1376–1384, 2012.
- [28] M. Luo *et al.*, "OriSnake: Design, fabrication, and experimental analysis of a 3-D origami snake robot," *IEEE Robot. Automat. Lett.*, vol. 3, no. 3, pp. 1993–1999, Jul. 2018.
- [29] S. Liu, G. Lu, Y. Chen, and Y. W. Leong, "Deformation of the Miura-ori patterned sheet," *Int. J. Mech. Sci.*, vol. 99, pp. 130–142, 2015.
- [30] H. Buri and Y. Weinand, "Origami-folded plate structures, architecture," in *Proc. 10th World Conf. Timber Eng.*, 2008, pp. 2–5.
- [31] J. Cai, Z. Ren, Y. Ding, X. Deng, Y. Xu, and J. Feng, "Deployment simulation of foldable origami membrane structures," *Aerosp. Sci. Technol.*, vol. 67, pp. 343–353, 2017.
- [32] J. Cai, Z. Qian, C. Jiang, J. Feng, and Y. Xu, "Mobility and kinematic analysis of foldable plate structures based on rigid origami," *J. Mechanisms Robot.*, vol. 8, no. 6, 2016, Art. no. 064502.
- [33] J. Cai, Y. Zhang, Y. Xu, Y. Zhou, and J. Feng, "The foldability of cylindrical foldable structures based on rigid origami," *J. Mech. Des.*, vol. 138, no. 3, 2016, Art. no. 031401.
- [34] J. Cai, X. Deng, Y. Zhou, J. Feng, and Y. Tu, "Bistable behavior of the cylindrical origami structure with Kresling pattern," *J. Mech. Des.*, vol. 137, no. 6, 2015, Art. no. 061406.

- [35] J. Cai, X. Deng, J. Feng, and Y. Zhou, "Geometric design and mechanical behavior of a deployable cylinder with Miura origami," *Smart Mater. Struct.*, vol. 24, no. 12, 2015, Art. no. 125031.
- [36] E. Richer and Y. Hurmuzlu, "A high performance pneumatic force actuator system: Part I—Nonlinear mathematical model," *J. Dyn. Syst. Meas. Control*, vol. 122, no. 3, pp. 416–425, 2000.
- [37] AKM[®]2G Servo Motor, Kollmorgen, Radford, VA, USA, 2017. [Online]. Available: <http://www.kollmorgen.com>. Accessed on: May 2018.



Jianshu Zhou (S'16) received the B.Sc. degree in automotive engineering with distinctive from Central Southern University, Changsha, China, in 2015, and M.Sc. degree in mechanical engineering with distinction from The University of Hong Kong, Pokfulam, Hong Kong, in 2016. He is currently working towards the Ph.D. degree in mechanical engineering at The University of Hong Kong.

His research interests include soft robots, bioinspired robots, robotic end effectors, and robotic grasping and manipulation.



Juan Yi received the B.Sc. degree in mechanical engineering from the Huazhong University of Science and Technology, Wuhan, China, in 2014. Since September 2014, She has been working towards Ph.D. at the department of Mechanical Engineering, studied in Robotics from the University of Hong Kong, Pokfulam, Hong Kong.

Her research interest includes soft robotics, human–robot interaction, and soft wearable robots.



Yujia Liu received the B.Sc. degree in measurement and control technology and instrument from the Huazhong University of Science and Technology, Wuhan, China in 2014, and the M.Sc. degree in mechanical engineering from The University of Hong Kong, Pokfulam, Hong Kong, in 2018.

Since 2018, she has been working mainly on soft robotic actuators and grippers with the Bionic Design and Learning Lab, Southern University of Science and Technology, Shenzhen, China.



Xiaojiao Chen (S'16) received the B.Eng. degree in mechanical engineering from the Huazhong University of Science and Technology, Wuhan, China, in 2012, and the M.S. degree in mechanical engineering from The University of Hong Kong, Pokfulam, Hong Kong, in 2015. He is currently working towards the Ph.D. degree in soft robotics at The University of Hong Kong.

His research interests include the field of soft actuators, soft robotic arms, variable stiffness control, and human–robot interaction.



Sicong Liu received the B.S.(Hons.) degree in mechanical design manufacturing and automation from the Harbin Institute of Technology, Harbin, China, in 2009, the M.S. degree in mechanical design and theory from the Harbin Institute of Technology in 2011, and the Ph.D. degree in robotics and engineering mechanics from Nanyang Technological University, Singapore, in 2012.

His research interests include deployable structures inspired by origami, mechanism for soft robotics, three-axis gimbal system, and design of humanoid robots.



Chaoyang Song received the B.Eng. degree in mechanical engineering from Tongji University, Shanghai, China, in 2009, and the Ph.D. degree in mechanism and robotics from Nanyang Technological University, Singapore, in 2014.

From March 2013 to November 2015, he was a Postdoctoral Research Fellow with the Massachusetts Institute of Technology and the Singapore University of Technology and Design. Then, he was a Lecturer (Assistant Professor) with the Department of Mechanical and Aerospace Engineering, Monash

University. He is currently an Assistant Professor with the Department of Mechanical and Energy Engineering and the Institute of Robotics, Southern University of Science and Technology, Shenzhen, China. His research interest includes the design science of bionic robotics and robot learning.



Zheng Wang (SM'16) received the B.Sc. degree in automatic control with merit from Tsinghua University, Beijing, China, in 2004, the M.Sc. degree in control systems with distinctive from Imperial College London, London U.K., in 2005, and the Ph. D degree in electrical engineering with merit from Technische Universität München, Munich, Germany, in 2010.

He was a Postdoctoral Research Fellow with the Nanyang Technological University, Singapore, between 2010 and 2013, and a Postdoctoral Fellow with the School of Engineering and Applied Sciences and the Wyss Institute of Bioinspired Engineering at Harvard University in 2013 and 2014. Since July 2014, he has been an Assistant Professor with the Department of Mechanical Engineering, The University of Hong Kong, Pokfulam, Hong Kong. His research interests include haptics human–robot interaction, endoscopic surgical robot, underwater robots, and soft robotics.